GJ 436b and the stellar wind interaction: simulations constraints using Ly α and H α transits

Carolina Villarreal D'Angelo [●],[1,2]★ Aline A. Vidotto [●],[1]★ Alejandro Esquivel [●],[3] Gopal Hazra [●][1] and Allison Youngblood[4]

[1]*School of Physics, Trinity College Dublin, College Green, Dublin-2, Ireland*
[2]*Observatorio Astronómico de Córdoba - Universidad Nacional de Córdoba. Laprida 854, X5000BGR Córdoba, Argentina*
[3]*Instituto de Ciencias Nucleares, Universidad Nacional Autónoma de México, Apartado Postal 70-543, 04510 Ciudad de México, Mexico*
[4]*Laboratory for Atmospheric and Space Physics, University of Colorado, Boulder, CO 80303, USA*

ABSTRACT

The GJ 436 planetary system is an extraordinary system. The Neptune-sized planet that orbits the M3 dwarf revealed in the Ly α line an extended neutral hydrogen atmosphere. This material fills a comet-like tail that obscures the stellar disc for more than 10 h after the planetary transit. Here, we carry out a series of 3D radiation hydrodynamic simulations to model the interaction of the stellar wind with the escaping planetary atmosphere. With these models, we seek to reproduce the $\sim$56 per cent absorption found in Ly α transits, simultaneously with the lack of absorption in H α transit. Varying the stellar wind strength and the EUV stellar luminosity, we search for a set of parameters that best fit the observational data. Based on Ly α observations, we found a stellar wind velocity at the position of the planet to be around [250–460] km s^{-1} with a temperature of [3–4] $\times$ 10^5 K. The stellar and planetary mass-loss rates are found to be 2 $\times$ 10^{-15} M$_\odot$ yr^{-1} and $\sim$[6–10] $\times$ 10^9 g s^{-1}, respectively, for a stellar EUV luminosity of [0.8–1.6] $\times$ 10^{27} erg s^{-1}. For the parameters explored in our simulations, none of our models present any significant absorption in the H α line in agreement with the observations.

Key words: line: profiles – methods: numerical – planets and satellites: individual: GJ 436b – planet–star interactions – stars: individual: GJ 436 – stars: winds, outflows.

1 INTRODUCTION

Just like the planets in our Solar system, exoplanets are immersed in the (magnetized) wind of their host stars. In particular, gas giant planets that orbit very close to their hosts (orbital distances $a_p <$ 0.5 au) experience a large stellar irradiation flux that causes the heating and expansion of the upper layers of their atmosphere. The atmospheric material then escapes in the form of a 'planetary wind' (Lammer et al. 2003).

The physical process involved in the interaction between the stellar and the induced planetary wind leaves an imprint that can be observed during planetary transits and can be modelled by means of numerical simulations. Comparing the model result with the observations allows us to constrain the parameters of the planetary system that are not directly determined by observations (Villarreal D'Angelo et al. 2014; Vidotto & Bourrier 2017; Villarreal D'Angelo et al. 2018; Kislyakova et al. 2019).

The Ly α line has become an important tool in this sense. This line has shown that in certain cases the amount of neutral hydrogen leaving the planet atmosphere can obscure a substantial part of the stellar flux during the planetary transit. One of the most extreme cases is that of the Neptune-mass exoplanet GJ 436b. For this exoplanet, an excess in absorption was detected first by Kulow et al. (2014) and later

confirmed by Ehrenreich et al. (2015). In this work, observations with the STIS spectrograph on board Hubble revealed that the absorption in Ly α at mid-transit reached 56.3 $\pm$ 3.5 per cent, almost 80 times larger than the absorption caused by the planet in broad-band optical transit (0.69 per cent). The Ly α absorption was observed to start $\sim$3 h before mid-transit, and to end more than 10 h after mid-transit (Bourrier et al. 2016; Lavie et al. 2017). This asymmetry indicates that the neutral hydrogen escaping GJ 436b takes the form of a comet-like tail.

The set of Ly α observations gathered for this exoplanet covering the planetary transit spans more than 5 yr (2012, 2013, 2014, and 2016; Kulow et al. 2014; Ehrenreich et al. 2015; Lavie et al. 2017). In most of them, a maximum absorption of $\sim$60 per cent in the blue wing of the line (defined between [−120, −40] km s^{-1}) occurring close to mid-transit, appears stable in the different epochs. On the contrary, the red wing defined between [30, 110] km s^{-1}, show a time variable absorption after mid-transit revealing the presence of transients either from stellar or planetary origin.

Numerical models have shown that the observational features found in Ly α can be explained with an evaporating atmosphere that expands several planetary radii behind the planet (Bourrier et al. 2016; Khodachenko et al. 2019; Kislyakova et al. 2019). All these models assume that, to some extent, radiation pressure, charge exchange, and the interaction with the stellar wind give rise and shape the neutral material that leaves the planet, giving the asymmetric shape of such absorption. Although it is clear by now

* E-mail: carolina.villarreal@unc.edu.ar (CVD); aline.vidotto@tcd.ie (AAV)

Table 1. GJ 436 system parameters. Stellar parameters taken from Torres (2007) and France et al. (2016). Planet parameters taken from von Braun et al. (2012).

Object	Symbol	Value
GJ 436	–	–
Mass ($M_\odot$)	$M_\star$	0.50
Radius ($R_\odot$)	$R_\star$	0.45
Distance (pc)	d	10.2
GJ 436b	–	–
Mass (M_J)	M_p	0.078
Radius (R_J)	R_p	0.36
semimajor axis (au)	a_p	0.03
Orbital period (d)	τ_p	2.64
Inclination (°)	i	86.6

that all of these physical process are in play, there is no consensus on which process play a major role (see Bourrier et al. 2016 and Khodachenko et al. 2019). Despite the differences, the main features of the observed Ly α absorption profile are well reproduced by the different models, mainly the sharp ingress and a long egress observed in the blue wing. However, none of the models developed so far can simultaneously render all the data acquired for this exoplanet with a single set of parameters. Moreover, parameters like stellar wind velocity or stellar and planetary mass-loss rate used to match the observational Ly α absorption of GJ 436b in the different models are still in disagreement, as we discuss next.

Multispecies hydrodynamic models either in 1D (Salz et al. 2016; Loyd et al. 2017) or 3D (Shaikhislamov et al. 2018; Khodachenko et al. 2019) agree with a planetary mass-loss rate of $3 \times 10^9\,\mathrm{g\,s^{-1}}$ and a planetary wind terminal velocity of $10\,\mathrm{km\,s^{-1}}$ to reproduce the observations. On the other hand, the particle simulations of Bourrier et al. (2016) and Lavie et al. (2017) predict a planetary wind velocity between [50–60] $\mathrm{km\,s^{-1}}$ and a mass-loss rate an order of magnitude lower.

The stellar wind parameters, such as density and velocity at the interaction region, are by-products of the Ly α escape modelling. Bourrier et al. (2016) and Vidotto & Bourrier (2017) estimated a stellar wind mass-loss rate between $[0.5–2.5] \times 10^{-15} M_\odot\,\mathrm{yr}^{-1}$. Vidotto & Bourrier (2017) found that an isothermal stellar wind temperature of [0.36–0.43] MK is needed to reproduce the local stellar wind velocity of $86\,\mathrm{km\,s^{-1}}$, estimated by Bourrier et al. (2016). Recently, Mesquita & Vidotto (2020) presented stellar wind models for GJ 436 that account for the presence of Alfvén waves to heat and accelerate the stellar wind. These authors derive a mass-loss rate of $<7.6 \times 10^{-15} M_\odot\,\mathrm{yr}^{-1}$, consistent with Bourrier et al. (2016), but a significantly higher stellar wind velocity with an upper limit of $800\,\mathrm{km\,s^{-1}}$ at the position of the planet.

With the exception of Mesquita & Vidotto (2020), who modelled only the wind of GJ 436, all the estimated parameters for the GJ 436 system have used only the Ly α observations to constrain the model results, as in-transit absorption in other spectral lines have not been detected. Cauley, Redfield & Jensen (2017) searched for H α in-transit absorption without success, despite the extraordinary absorption of the neutral hydrogen in the Ly α line. For the more heavy species like C II and Si III, Loyd et al. (2017) were able to put an upper limit to the expected absorption based on a numerical model.

In this work we seek to constrain the stellar and planetary wind properties of GJ 436 by modelling the stellar and planetary wind interaction and computing synthetic Ly α and H α transits, to be compared to the observations. Table 1 summarizes the physical

properties of this system. We employ a 3D radiative hydrodynamic code to model the propagation and interaction of stellar and planetary winds exploring different parameters. The stellar wind of the GJ 436 is determined by setting the coronal temperature of the star and the mass-loss rate. The planetary wind is fully determined by the amount of EUV flux (F_{EUV}), derived from observations, that the atmosphere receives. The wind from the planet is modelled with a 1D code that solves the atmospheric escape process from the lower planetary atmosphere (Allan & Vidotto 2019), and provides the boundary conditions in the 3D model. The same F_{EUV} value is used in both the 1D and 3D models. In this way, a consistent set of initial parameters is used to explore the wind–wind interaction in this exoplanetary system. With this, we obtain the observational signatures in both H α and Ly α lines during transit, and compare those to previous observations.

The paper is organized as follows: Section 2 introduces the numerical code with all the physical process involved. In this section we explain the boundary conditions used in the simulations to reproduce the stellar and planetary wind. Section 3 presents the results from our models and Section 4 the computation of the synthetic H α and Ly α lines. We present a summary of our results in Section 5 and a discussion about the caveats in our modelling approach – for example, our model includes radiation pressure (investigated in Appendix A), but does not include charge exchange processes. We present our conclusions in Section 6.

2 SIMULATIONS

To simulate the GJ 436 planetary system we employ the hydrodynamics/magnetohydrodynamics-radiative code GUACHO.[1] GUACHO has already been employed in several works to simulate the interaction of stellar and planetary wind of the HD 209458 system (Schneiter et al. 2016; Villarreal D'Angelo et al. 2018; Esquivel et al. 2019). We have made use of the hydrodynamic version of the code that solves the following set of equations:

$$\frac{\partial \rho}{\partial t} + \nabla \cdot (\rho \boldsymbol{u}) = 0, \tag{1}$$

$$\frac{\partial (\rho \boldsymbol{u})}{\partial t} + \nabla \cdot (\rho \boldsymbol{u}\boldsymbol{u} + \mathbf{I}P) = \rho(\boldsymbol{g}_p + \boldsymbol{g}_{e,\star}), \tag{2}$$

$$\frac{\partial E}{\partial t} + \nabla \cdot [\boldsymbol{u}(E + P)] = G_{rad} - L_{rad} + \rho\left(\boldsymbol{g}_p + \boldsymbol{g}_{e,\star}\right) \cdot \boldsymbol{u}, \tag{3}$$

where ρ, $\boldsymbol{u}$, P, and E are the mass density, velocity, thermal pressure, and energy density, respectively. $\mathbf{I}$ is the identity matrix, while G_{rad} and L_{rad} the gains and losses due to radiation. $\boldsymbol{g}_{e,\star}$ and $\boldsymbol{g}_p$ are the (effective) stellar and planetary gravitational acceleration. The total energy density and thermal pressure are related by an ideal gas equation of state $E = \rho |\boldsymbol{u}|^2/2 + P/(\gamma - 1)$, where $\gamma = 5/3$ is the ratio between specific heat capacities.

The hydrodynamics equations (left-hand side of equations 1–3), are advanced with a second-order Godunov method with an approximate Riemann solver (HLLC; Toro 1999), and a linear reconstruction of the primitive variables using the minmod slope limiter to ensure stability.

The numerical setup have the star and the planet within the computational domain with the planet orbiting around the star in the xz-plane. Our physical domain covers [0.15, 0.03, 0.75] au ($\sim$65$R_\star$ in the *x*-direction) divided in 880 × 176 × 460 cells in the *x*, *y*, and *z* direction, respectively, as we only simulate half of the orbital

---

[1]Freely available in https://github.com/esquivas/guacho
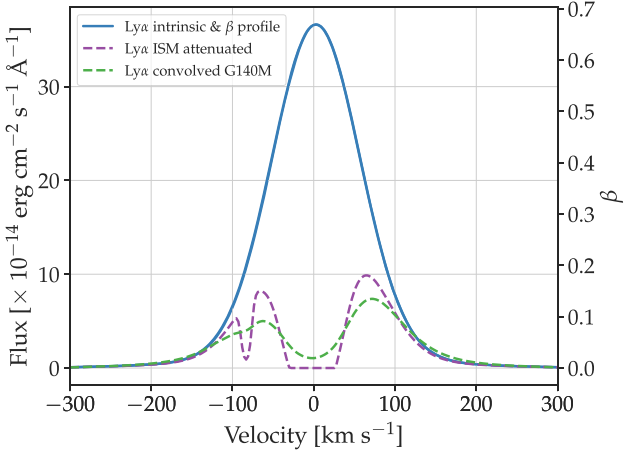
Figure 1. GJ 436 intrinsic Ly α flux at Earth obtained from the MUSCLES survey and the corresponding β profile used to calculate the radiation pressure force in our simulations (blue solid line). The dashed lines correspond to flux attenuated by the ISM (violet) and then convolved with the G140M grating response of the *HST* STIS instrument (green).

plane. With this, our resolution is about 1.7×10^{-4} au ($\sim 0.07 R_\star$). By simulating only half of the orbit, and imposing the axisymmetric nature in the numerical setup, we can save computational resources. Our simulations take 60 core-hours in 84 cores to complete.

2.1 Source terms

The right-hand side of equations (1) to (3) are our source terms, which represent all the external quantities that make the equations non-conservative. In our numerical scheme, they are included after each time-step. These terms are described next.

2.1.1 Gravity and radiation pressure

In our simulations the gravity forces from the star and the planet are included as that of two point sources. We also include the effect of stellar radiation pressure as in Esquivel et al. (2019), and so the gravity of the star is reduced by a factor proportional to the flux in the Ly α line and the neutral fraction. The effective stellar gravity is then

$$g_{e,\star} = (1 - \beta(v)\chi_n)g_\star, \qquad (4)$$

with χ_n the total neutral fraction inside each grid cell and $\beta(v)$ a velocity-dependent parameter proportional to the flux in the line. To compute $\beta(v)$ we employ the formula presented in Lagrange et al. (1998) and the reconstructed flux of GJ 436 in the Ly α line taken from the MUSCLES survey (France et al. 2016; Loyd et al. 2016; Youngblood et al. 2016). The implementation of the radiation pressure in our simulations neglects self-shielding. Because of this, the radiation pressure force can be overestimated. We analyse the consequence of this in Section 5.1 and address this point in more detail in Appendix A2.

The intrinsic Ly α flux at Earth and the resulting β profile used in our simulations is shown in Fig. 1 (solid blue line). The figure also shows the attenuated profile due to the ISM absorption (violet line) and the one resulting from the convolution with the G140M grating from *HST* (green line), that will be used to simulate an observation with the STIS instrument during transit with our models (Fig. 6).

Table 2. Rate coefficients of 'case B' recombination and collisional ionization reaction implemented our simulations.

$\alpha(T)$	$2.55 \times 10^{-13}(10^4/T)^{0.79}$	Osterbrock (1989)
$c(T)$	$5.83 \times 10^{-11}\sqrt{T}\exp(-157828/T)$	Osterbrock (1989)

The Ly α intrinsic profile taken from Youngblood et al. (2016) uses an H I column density of $N_{HI} = 1.1 \times 10^{18}$ cm^{-2}, a velocity centroid $v_{HI} = -4.1$ km s^{-1} and Doppler parameter $b_{HI} = 8.6$ km s^{-1} to model the ISM H I absorption. For the deuterium absorption, we use the ratio D I/H I = 1.5×10^{-5} (as in Wood et al. 2004), the same velocity centroid as v_{HI}, and we assume $b_{DI} = b_{HI}/\sqrt{2}$.

This reconstructed Ly α line has a total flux of $F_{Ly\alpha} = (2.1 \pm 0.3) \times 10^{-13}$ erg cm^{-2} s^{-1}, which gives a $F_{Ly\alpha} = 0.92$ erg cm^{-2} s^{-1} at 1 au in agreement with Ehrenreich et al. (2015). The luminosity values used in our simulations are based in this $F_{Ly\alpha}$ value (see Section 2.2).

2.1.2 Radiative processes

Within our models, the neutral hydrogen can be ionized by collisions or EUV photons and is allowed to recombine from an ionized state. To follow the change of neutral hydrogen within our simulations we solve the following equation after every hydrodynamic step:

$$\frac{\partial n_{HI}}{\partial t} + \nabla.(n_{HI}\boldsymbol{u}) = (n_H - n_{HI})^2\alpha(T)$$
$$- (n_H - n_{HI})n_{HI}c(T) - n_{HI}\phi, \qquad (5)$$

where $n_H = \rho/m_H$ is the total hydrogen number density ($m_H = 1.66 \times 10^{-24}$ g being the hydrogen mass) and n_{HI} is the number density of neutral hydrogen. $\alpha(T)$, c(T) are the 'case B' recombination and collisional ionization rates presented in Table 2. The photoionization rate, ϕ is computed through the rate of ionizing photons (S) that reach a cell volume. Hence, $\phi = S/(n_{HI}dV)$, where $S = S_0\exp(-n_{HI}a_0 dl)$ is the ionizing photon-rate which is attenuated as the photons are absorbed in their propagation through the grid, $a_0 = 6.3 \times 10^{-18}$ cm^2 is the photoionization cross-section at the threshold frequency (13.6 eV h^{-1}) and dl is the path that the photon travels, taken in steps of one half of the cell size. S_0 is the initial photon-rate value set by the stellar luminosity in the EUV. In our models, we calculate the initial value of S_0 by dividing the total luminosity value in the EUV range by 13.6 eV.

To launch the stellar photons, we employ the ray-tracing method described in Esquivel & Raga (2013), with 10^7 photon-packages being ejected from the star at a random position from its surface, and in a random outward direction. Each photon package is followed and absorbed within a cell every time they find neutral material. As the photons moves, we keep track of the ionizing rate at each cell and the energy deposited to the flow. Since we are simulating half of the planet orbit, hence half of the star, the value of S_0 is divided by 2 (with all the photons imposed only from the hemisphere within the domain).

2.1.3 Heating and cooling

The incoming stellar radiation will heat the planetary wind due to photoionization. Assuming that all the photoelectrons produced during this processes will heat the gas, the volumetric heating rate can be expressed as

$$G_{rad} = n_{HI}\int_{v_0}^\infty \frac{4\pi J_v}{hv}a_v e^{-\tau_v}h(v - v_0)dv, \qquad (6)$$

where n_{HI} is the neutral density, $4\pi J_\nu$ is the average intensity of the stellar radiation, ν_0 is the threshold frequency (13.6 eV h^{-1}), a_ν is the photoionization cross-section and $\tau_\nu = \int a_\nu n_{HI} dl$ is the absorption of the stellar flux as it moves within the neutral material. Equation (6) can be solved numerically when the stellar spectral energy distribution is known. In our case, to reduce computational time, we treat the stellar flux as monochromatic, with this, the absorption cross-section ($a_\nu = 6.3 \times 10^{-18}(\nu/\nu_0)^3$) becomes $a_0 = 6.3 \times 10^{-18}$ cm^2 (Osterbrock 1989). In this case, equation (6) becomes

$$G_{rad} = n_{HI}\phi\epsilon, \qquad (7)$$

where ϕ is the photoionization rate and $\epsilon = (h\nu - h\nu_0)$ is the average energy gain per photoionization. In our models, we assume $\epsilon \sim 2$ eV, meaning that the stellar flux is composed of photons with energy of ~ 15.6 eV given a heating efficiency of $(h\nu - h\nu_0)/h\nu \sim 0.1$. Heating efficiencies for planets with hydrogen-dominated atmospheres where calculated in the work of Shematovich, Ionov & Lammer (2014), where it was found that a value of 0.2 was almost constant within the planet thermosphere. On the other hand, Yelle (2004) found that the heating efficiency decreased from 0.5 up to 0.1 within the planetary atmosphere, expecting to be small above $\sim 2R_p$ due to the escape of photoelectrons from the planetary atmosphere. Our choice of a heating efficiency of ~ 0.1 reflects this idea since our boundary condition to launch the planetary wind start at $5R_p$.

The assumption of a monochromatic flux is quite useful in 3D simulations, as it reduces computational time. This assumption has been used in a series of works (e.g. Murray-Clay, Chiang & Murray 2009; Debrecht et al. 2019; McCann et al. 2019). For example, Debrecht et al. (2019) assume that stellar photons have a single energy of 16 eV, which is representative of the integrated EUV flux from the Sun (Trammell, Arras & Li 2011). Recently, Hazra, Vidotto & D'Angelo (2020) showed that a monochromatic flux gives a similar solution for the planetary wind as that computed using a non-monochromatic case, and so, our choice of a stellar monochromatic flux is fairly justified.

The non-equilibrium cooling function due to radiative processes, L_{rad}, used in our models is taken from the work of Biro, Raga & Canto (1995):

$$L_{rad} = L_{ion} + L_{Ly_\alpha} + (1 - f)[L_{rec} + A(L_{O_I} + L_{O_{II}})] + f L_{equil}. \quad (8)$$

The total volumetric cooling rate is then the contribution from the cooling due to collisional ionization (L_{ion}), collisional excitation of the Ly α line (L_{Ly_α}), and recombination (L_{rec}).

Additionally, cooling due to the collisional excitation of the forbidden O$_I$ and O$_{II}$ lines ($L_{O_I}, L_{O_{II}}$) is included, and is multiplied by a factor $A = 7.033$, to account for the contribution of other important ions that produce cooling such as C, N, and S (see the work of Biro et al. 1995 for details). We do not include photoionization heating by these metals as our 3D simulations start at $5R_p$. Photoionization of metals could become important lower in the planetary thermosphere, but for a solar abundance composition the error introduced by neglecting them should be smaller than the uncertainty in the EUV flux value (Salz et al. 2015, 2016).

For temperatures higher than 5×10^4 K, the cooling function in equation (8) approaches the cooling of an ionized gas in coronal equilibrium (L_{equil}). This is done through the function $f(T) = \frac{1}{2}(\frac{1+\tanh(T-5\times10^4)}{500K})$ which allows us to switch from the low temperature regime to a higher one. The parametrization of L_{equil} can be found in Raga & Cantó (1989) and includes the free–free cooling.

Our cooling function is not valid for temperatures lower than 1×10^4 K and therefore, we turn-off the cooling below this temper-

ature. This may not be realistic as the planetary wind temperature at the boundary of the planet is in all models of the order of 10^3 K. However, we assume that the contribution of the radiative cooling at this temperature is not significant and the material will cool mostly as a consequence of the planetary wind expansion (adiabatic cooling). Note that, we do not include cooling by H$_3^+$, as molecular hydrogen is found in the lower layers of the atmosphere ($<1\,\mu$bar; Koskinen et al. 2013), which are not included in our computation.

2.2 Boundary conditions

The stellar and the planetary winds are treated as inner boundary conditions in our global 3D simulations. At the position where the wind is launched we set the values for temperature, velocity, neutral fraction, and total density (through the corresponding mass-loss rate) for a purely hydrogen fluid. These values are then re-imposed at every time-step. The outer boundary conditions, i.e. the boundaries at the end of the mesh, are treated as outflow except for the boundary at the x- axis. This boundary is set to a reflective boundary to mimic the axisymmetric nature of the system, as we only model half of the orbital plane.

2.2.1 Stellar wind and photoionizing flux

The boundary conditions for the stellar wind are given by a Parker wind solution for a coronal temperature $T_\star$:

$$v_r \exp\left[-0.5\left(\frac{v_r}{c_s}\right)^2\right] = c_s \left(\frac{r_c}{r}\right)^2 \exp\left(\frac{-2r_c}{r} + \frac{3}{2}\right). \qquad (9)$$

Here $r_c = GM_\star/(2c_s^2)$ is the position of the critical point where the velocity of the wind equals the sound speed $c_s = \sqrt{R_g T_\star/\mu}$, with R_g the gas constant and $\mu = 0.5$ the mean atomic weight of the particles in units of m_H. In this work, we vary the coronal temperature of the star between 1 and 3 MK to simulate different stellar wind strengths at the planet position. In the Parker wind model, the higher the temperature of the wind, the higher is the stellar wind velocity. We chose temperatures in this interval to cover values previously suggested in the literature. For example, in Vidotto & Bourrier (2017), an isothermal temperature of the stellar wind is estimated to be 0.41 MK, while in Mesquita & Vidotto (2020), the predicted stellar wind temperature at the planetary orbit is $\lesssim 1.7$ MK, but can reach higher values at larger distances from the star.

In our models, the launching radius, r_{sw}, for the fully ionized stellar wind is set above or at the sonic point and the velocity at this radius is determined by equation (9). The choice of the launching radius help us save computational resources and allow us to use an adiabatic index ($\gamma = 5/3$) to properly model shocks. More sophisticated stellar wind models include extra terms in the energy and momentum equations to heat and accelerate the stellar wind from the stellar radius when adopting $\gamma = 5/3$ (Mesquita & Vidotto 2020).

Note that the Parker solution is isothermal ($\gamma = 1$), while our models assume an adiabatic index. This means that the stellar wind cools down as it expands in the grid, with the highest temperature at r_{sw}, and thus the temperatures quoted at the orbital distance of the planet are lower than their injection values of 1 to 3 MK (see Table 3).

The density at the boundary is set by the adopted mass-loss rate of the star. Previous works (Vidotto & Bourrier 2017; Mesquita & Vidotto 2020) estimated for GJ 436 a mass-loss rate of [0.03–0.8] $\dot{M}_\odot$, with the solar mass-loss rate given by $\dot{M}_\odot = 2 \times 10^{-14}$ M$_\odot$ yr^{-1}.

Table 3. Physical quantities adopted for the star and its wind. All the stellar wind models assume a mass-loss rate of $2 \times 10^{-15} M_\odot \, \text{yr}^{-1}$. The columns are: the model name, the stellar wind temperature at its launching radius, the EUV luminosity of the star, the velocity, temperature, and density of the stellar wind at the orbital radius of the planet. Model names indicates the intensity of the stellar EUV luminosities: H (high), M (moderate), and L (low), and the chosen stellar wind temperature: 1 correspond to $T_\star = 1$ MK and 3 to $T_\star = 3$ MK.

Model –	$T_\star$ $(10^6 \, \text{K})$	L_{EUV} $(10^{27} \, \text{erg s}^{-1})$	$v(a_p)$ (km s^{-1})	$T(a_p)$ $(10^5 \, \text{K})$	$n_H(a_p)$ (cm^{-3})
L1	1	0.8	254	4	11 661
M1	1	1.6	254	4	11 661
H1	1	4	199	2	1542
L3	3	0.8	465	3	634
M3	3	1.6	465	3	634
H3	3	4	465	3	634

Thus, we assume $\dot{M}_\star = 0.1 \dot{M}_\odot$ in our models. For a given mass-loss rate and considering an isotropic wind, this implies that the density at the wind boundary is $\rho(r_{\text{sw}}) = \dot{M}_\star / (v(r_{\text{sw}}) 4\pi r_{\text{sw}}^2)$, with $v(r_{\text{sw}})$ determined according to the chosen stellar wind temperature (equation 9).

The photoionizing flux is simulated with the emission of photons from the surface of the star. We launch a total of 10^7 photons packages in random directions from random positions on the stellar surface. The initial photon-rate (S_0) is set through the EUV luminosity L_{EUV} adopted for GJ 436. Ehrenreich et al. (2015) estimated a luminosity around $[2.8–3] \times 10^{27} \, \text{erg s}^{-1}$ (calculated in the range [124–912] Å). Based on the Ly α line and the scaling relations from Linsky, Fontenla & France (2014), Youngblood et al. (2016) estimated a $L_{\text{EUV}} = 1.7 \times 10^{27} \, \text{erg s}^{-1}$ in the same wavelength range. More recently, Peacock et al. (2019) derived a luminosity value of $4.9 \times 10^{27} \, \text{erg s}^{-1}$, calculated in the range [124–912] Å.

For our models, we have chosen to explore three different values of $L_{\text{EUV}} = [0.8, 1.6, 4] \times 10^{27} \, \text{erg s}^{-1}$, which span a factor of 5 in luminosity and cover the range of literature EUV estimates for this star. Based on these values, we have named our models with the letter L for low, M for moderate, and H for high, respectively. For the three luminosity values we chose, the photoionization time of hydrogen near the interaction region (shock position), in the star–planet direction, varies from 28 to 8 h for the lowest and the highest L_{EUV} values, respectively. These values change to 8 and 2 h in the planetary tail. We note that we do not change the Ly α flux used to calculate the radiation pressure in our models while varying L_{EUV}, because this value is constrained by direct observations to be relatively constant over a period of several years (e.g. Ehrenreich, Lecavelier Des Etangs & Delfosse 2011; France et al. 2013; Youngblood et al. 2016; Lavie et al. 2017).

All the physical values adopted for the star and its wind are presented in Table 3, together with the resulting values of the stellar wind at the planet orbit.

2.2.2 Planetary wind

Similar to the stellar wind, the planetary wind is launched at a given radius, r_{pw}, where the velocity, temperature, density, and ionization fraction are set. These parameters are taken from the 1D hydrodynamic atmospheric escape model presented in Allan & Vidotto (2019) and rendered uniformly around the planet at the launching radius. In this model, a planetary wind is generated from
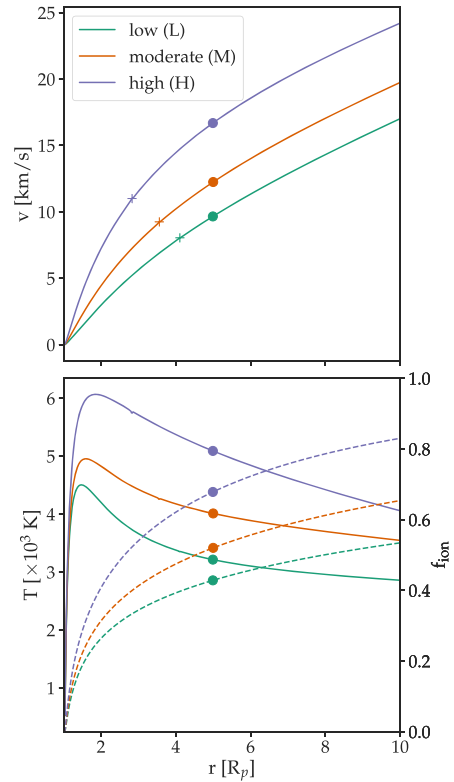

Figure 2. Planetary wind profiles for three different values of the stellar EUV flux (low, moderate, and high) from the 1D atmospheric model of Allan & Vidotto (2019). Top: radial velocity. Bottom: Temperature and ionization fraction. The dot represents the position of the boundary condition in the 3D model. The crosses in the velocity profile show the position of the sonic point.

the heating and expansion of the upper planetary atmosphere as a consequence of the photoionizing EUV flux from the star. The model takes as inputs the mass of the star, mass and radius of the planet, as well as the stellar EUV flux. For the escape model we also assume a density and a temperature at the bottom of the planetary atmosphere, which do not have a strong impact on the planetary wind profiles (see Allan & Vidotto 2019 and reference therein).

Using the values of L_{EUV} shown in Table 3, we create three different planetary wind models with the 1D escape model. The radial profiles of velocity, temperature, and ionization fraction (f_{ion}) for the three models are shown in Fig. 2. In the figure, model names correspond to the high (H), moderate (M), and low (L) stellar EUV luminosity. The values used at r_{pw} are marked with a dot and also stated in Table 4. In the velocity profile the position of the sonic point for each of the planetary wind models is marked with a cross. Note that to keep the resolution in the 3D simulation in a reasonable value, we launch the planetary wind beyond the sonic point. The planetary wind models generated in this way have an ionization fraction of [0.4, 0.5, 0.7] at r_{pw} and a mass-loss rate of $[5.5, 9.8, 20] \times 10^9 \, \text{g s}^{-1}$ for the low, moderate, and high L_{EUV}, respectively.

We can compare our results with other atmospheric escape models. For example, Salz et al. (2016) estimated a mass-loss rate of $4 \times 4.4 \times 10^9 = 1.8 \times 10^{10} \, \text{g s}^{-1}$ for a $L_{\text{EUV}} = 1.4 \times 10^{27} \, \text{erg s}^{-1}$ (Salz et al.'s expression for $\dot{M}_p$ has a factor of 1/4 compared to ours). Their model should be compared to our model M, as they have similar L_{EUV} values. When comparing to our value of $9.8 \times 10^9 \, \text{g s}^{-1}$, we see that our mass-loss rate is comparable (within less than a factor of 2). For similar L_{EUV} values, Loyd et al. (2017) and Shaikhislamov

Table 4. Models boundary conditions. The model names correspond to the high (H), moderate (M), and low (L) stellar luminosity and to the high (3MK) and low (1MK) stellar wind base temperatures.
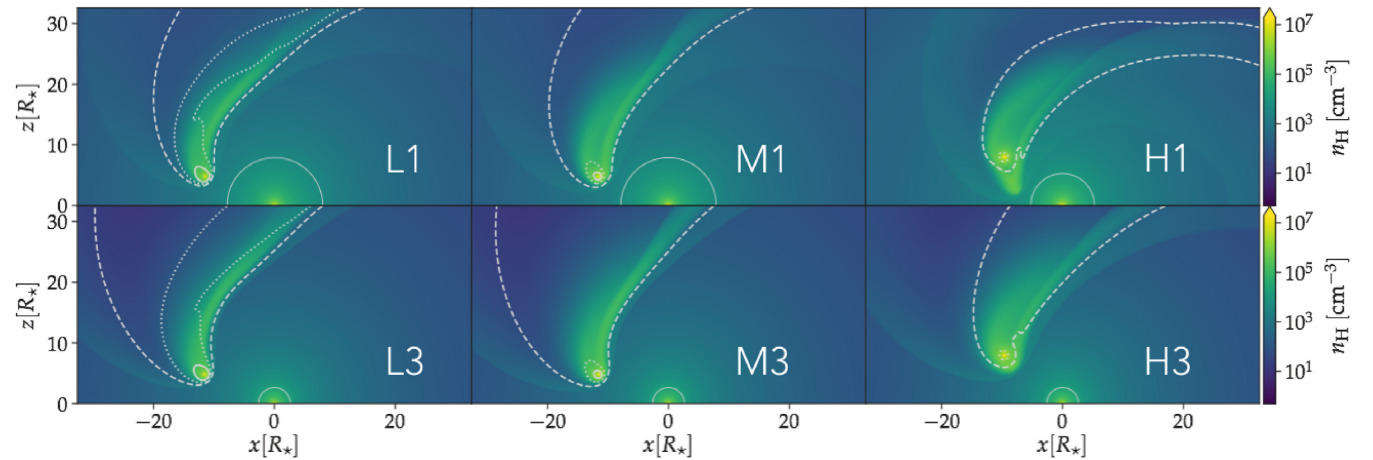
Parameter	L1	L3	M1	M3	H1	H3
Stellar wind						
r_{sw} ($R_\star$)	7.9	2.6	7.9	2.6	5.3	2.6
$T_\star$ (10^6 K)	1	3	1	3	1	3
$\dot{M}_\star$ ($\dot{M}_\odot$)	0.1	0.1	0.1	0.1	0.1	0.1
v_{sw} (km s^{-1})	181	313	181	313	130	313
L_{EUV} (10^{27} erg s^{-1})	0.8	0.8	1.6	1.6	4	4
S_0 (10^{36} s^{-1})	5.0	5.0	9.6	9.6	24.3	24.3
Planetary wind						
r_{pw} (R_p)	5	5	5	5	5	5
T_{pw} (K)	3212	3212	4008	4008	5086	5086
$\dot{M}_p$(10^9 g s^{-1})	5.5	5.5	9.8	9.8	20	20
v_{pw} (km s^{-1})	9.7	9.7	12.0	12.0	16.7	16.7
$f_{ion, pw}$	0.43	0.43	0.52	0.52	0.68	0.68

et al. (2018) found mass-loss rates of 3.1×10^9 and 4×10^9 g s^{-1}, respectively. Again, comparing to our model M, we see that their values are similar to ours (about a factor of 2 smaller).

3 3D MODELLING RESULTS

In order to characterize the environment around GJ 436b, we run six simulations. Three of them explore different values of L_{EUV} from the star, giving rise to three different planetary winds. These simulations are labelled with the letters L, M, and H. For each of these simulations we adopt two different stellar wind models corresponding to two values of stellar wind base temperature: 1 and 3 MK. The initial conditions used in our models are presented in Table 4.

Fig. 3 shows cuts of neutral hydrogen distribution in the orbital plane (xz) for all our simulations. The radius from where the stellar wind is launched, r_{sw}, is marked with a white circle around the position of the star (origin of coordinates). The models are evolved until they reach a steady state and we show in Fig. 3 the evolution of the simulation up to $t = 97\,200$ s, except for models H1/H3 where $t = 86\,400$ s for reasons we will present later. This corresponds to a temporal evolution of approximately 2/5 of an orbit.

As the planetary and stellar winds expand and interact in our simulations, common features arise in all cases. On one hand, a shock is formed at the position where the two winds meet. In the shocked region, the temperature increases to around 1 and 3 MK (depending on the model), as is visible from Fig. 4 where temperature contour is shown in the orbital plane for model L3, together with iso-surfaces of neutral hydrogen around the planet. These high temperatures ionized the planetary material shaping the region of neutrals between the star and the planet.

Another common feature is the development of a comet-like tail of escaping material trailing the planet. The extension of this tail vary according to the stellar wind strength. A stronger stellar wind ($T_\star = 3$ MK, bottom row of Fig. 3) pushes the material in the tail towards the radial direction, whereas a slower stellar wind ($T_\star = 1$ MK, top row of Fig. 3) allows the material to remain in the orbital path (i.e. the tail is more curved along the ϕ direction).

The amount of neutral material in the tail is controlled by the stellar EUV flux. A higher L_{EUV} increases the value of the ionization fraction at the boundary where the planetary wind is launched (see Table 4). Then the neutral material that eventually escapes within the tail becomes ionized when interacting with the stellar photons. The overall result is that a higher stellar L_{EUV} produces a more ionized tail. This can be seen if we focus on the white contours on Fig. 3 that show the values of ionization fraction [0.6, 0.8, 0.99], represented by the solid, dotted, and dashed lines around the planet, respectively.

As is visible from Fig. 3, model H1 (which is the one with the weakest stellar wind and the strongest planetary wind) developed a stream of material from the planet in the direction of the star. This is the result of a stellar wind being incapable of halting planetary material that moves towards the star. Hence, the planetary wind that gets more acceleration due to the high EUV flux is also accelerated by the stellar gravity and falls into the star ahead of the planet. This effect has already been studied by Carroll-Nellenback et al. (2017) and Matsakos, Uribe & Königl (2015).

This model has the higher planetary wind velocity and temperature at the launching radius (r_{pw}) due to the high stellar L_{EUV} (see Fig. 2). The stellar wind in model H1 is imposed at a smaller radius ($r_{sw} = r_c$) with respect to models L1 and M1. We choose this radius to let the simulation evolve at roughly the same physical time of all the others models, before the planetary material reaches the stellar wind boundary. Because of this, the velocity and temperature of model H1
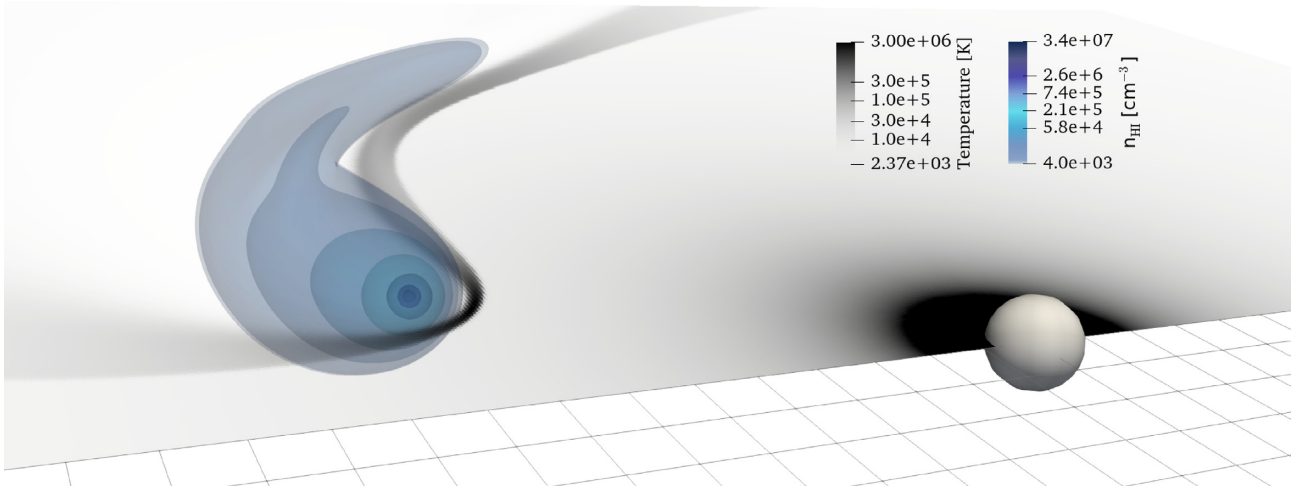
Figure 3. Cut in the orbital plane for $t = 97\,200$ s except for models H1 and H3 were $t = 86\,400$ s. The plots show the distribution of total hydrogen density for all the models. Top row: models with $T_\star = 1$ MK. Bottom row: models with $T_\star = 3$ MK. From left to right models with increasing stellar EUV flux. The white half-circle shows the launching radius of the stellar wind. The contours levels show the ionization fraction of 0.6, 0.8, and 0.99 from inside to outside.

Figure 4. 3D render view of model L3 at $t = 97\,200$ s. The orbital plane is coloured with temperature, while the contours around the planet represent the neutral H density. The shock is the high temperature region in front of the planet.

Table 5. Physical parameters adopted in the computation of the synthetic Ly α and H α transits.

Parameter	Ly α	H α
λ_0 (cm)	1.215668×10^{-5}	6.56279×10^{-5}
σ_0 (cm^2)	0.01105	0.017014
A_{ij} (s^{-1})	6.27×10^8	4.4101×10^7

are lower at the planetary position than models with the same initial base temperature, and so, this model has a lower total stellar wind pressure than models L1 and M1 (see Table 3 and Section 2.2).

It is important to point out that the change in the position of the boundary condition for the stellar wind does not affect the outcome of the infalling material. We saw the same result for a boundary at 1.5 r_c (not shown here).

4 SPECTROSCOPIC TRANSITS – SYNTHETIC LINE PROFILES

4.1 Ly α calculation

To calculate the Ly α absorption produced by our models, we compute the optical depth as a function of velocity along the line of sight (LOS) for each cell in the grid accounting for the orbital inclination of GJ 436b ($i = 86.6°$):

$$\tau_v = \int_{r_0}^{r} \sigma_0 n_{HI} W(a, v) dr_{LOS}. \tag{10}$$

Here, σ_0 is the absorption cross-section coefficient in the Ly α line at the threshold frequency (13.6 eV h^{-1}), n_{HI} is the neutral density, $W(a, v)$ is the Voigt line profile, and r_{LOS} is the path along the LOS. The integration is done from above the stellar wind launching radius to the end of the computational mesh.

The Voigt profile $W(a, v) = H(a, v)/\sqrt{\pi}$ is written in terms of the Humileck function which depends on the damping parameter $a = A_{ij}\lambda_0/(4\pi v_{th})$, and $v = (v_r - v_{LOS})/v_{th}$. Here A_{ij} is the transition rate, $\lambda_0 = 1215.67$ Å is the central wavelength of the line, $v_{th} = \sqrt{2k_B T/m_H}$ is the thermal width, v_r is the radial velocity which goes from $+300$ to -300 km s^{-1} in 250 bins and v_{LOS} is the velocity in the LOS direction. The line parameters are shown in Table 5.

To calculate the transmission spectra we integrate the normalized intensity within the stellar radius, neglecting any limb-darkening variation and so, the absorption spectra is $1 - I_v/I_\star = 1 - e^{-\tau_v}$. The total absorption is then the integration in the velocity range ± 300 km s^{-1}.

Because we only simulate half of the orbit and our analysis is done at the end of our simulation, we emulate the temporal evolution of the transit by rotating the LOS direction (z-axis) around the $-y$-axis (out of the page) in a clockwise direction, i.e. towards the x-axis. In this way, every angle swept by the LOS direction represent a time that can then be measured from mid-transit ($t = 0$). We stop our line profile calculations at an angle of 45°, which corresponds to 4 h after mid-transit. After this, part of the comet-like tail would have been outside the simulation domain and thus not contributing to the absorption line.

Following the approach from Lavie et al. (2017), we integrate the absorption in the Ly α line in two velocity ranges: the blue wing $[-120, -40]$ km s^{-1} and the red wing $[30, 110]$ km s^{-1}. The results of the two integrations are shown in Fig. 5 for all the models as a function of time from mid-transit. The figure also shows the duration of the optical transit in the grey stripe and the observations made in the different epochs extracted from Lavie et al. (2017) (blue and red triangles).

4.1.1 Blue wing absorption ($[-120, -40]$ km s^{-1})

As shown in the left-hand panel of Fig. 5, models with low and moderate L_{EUV} show the best agreement with the observations. Models L1/L3 and M1/M3 present highly asymmetric light curve with a long egress phase, due to the amount of neutral material within the comet-like tail. The duration and maximum depth of the absorption produced by this material is in good agreement with the observational results. These models, however, cannot reproduce the early ingress absorption observed 2 h before mid-transit. This is because the neutral material does not extend ahead of the planet, implying that, in these simulations, the interaction between the stellar and planetary wind is produced close to the planet position. We also see that the slope in the light curve at the ingress seems to depend on the strength of the stellar wind, a higher coronal temperature (i.e. a stronger wind) produces a steeper slope.

The maximum absorption values found for models L1/L3 and M1/M3 span a range from 50 to 80 per cent. This spread is related to
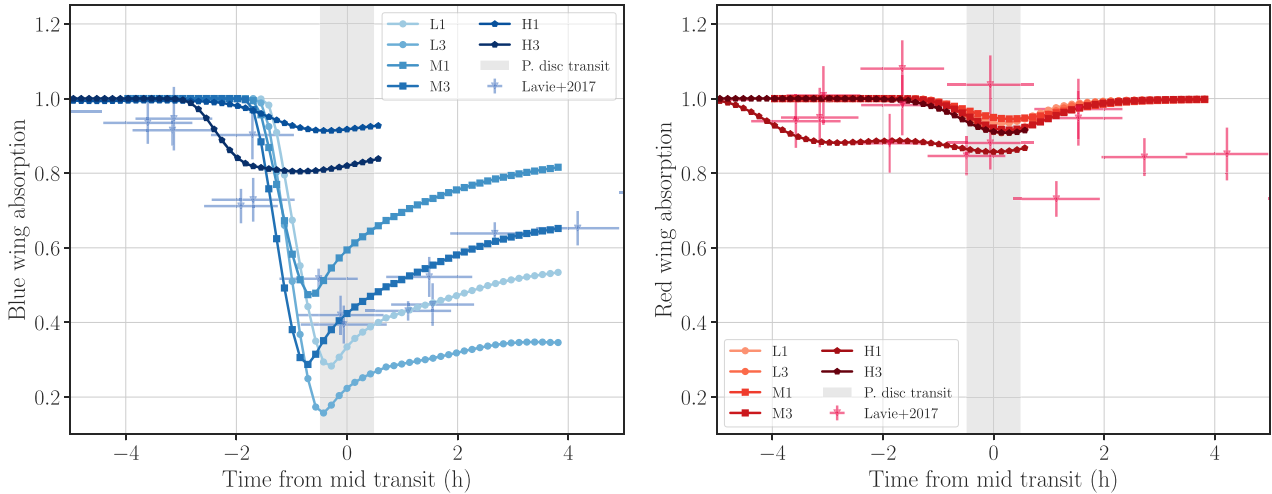
Figure 5. Blue and red wing Ly α absorption as a function of time for all the models together with the observations from Lavie et al. (2017). The grey band shows the duration of the optical transit.

the amount of neutral material that escapes from the planet, which is larger for the lowest stellar EUV flux ($L_{\mathrm{EUV}} = 0.8 \times 10^{27} \, \mathrm{erg \, s^{-1}}$).

Models with the highest stellar flux ($L_{\mathrm{EUV}} = 1.6 \times 10^{27} \, \mathrm{erg \, s^{-1}}$), H1 and H3, have the shallowest absorption, with values smaller than 20 per cent. Although these models present an absorption that begins around 2 h before mid-transit (being model H3 the earliest one), these models do not shown a long absorption duration, neither the $\sim$56 per cent of absorption seen in the observations at mid-transit. This is due to the high ionization fraction of the planetary wind, caused at the same time by the high L_{EUV}. Even though these models also show an extended comet-like tail, the amount of neutral material in this tail is too low to create sufficient absorption in this part of the line.

In all cases, models with the same EUV flux have a largest absorption when the stellar wind temperature is highest. This is because a stronger stellar wind confines more efficiently the neutral material in the radial direction and then the column density of this material increases in this direction.

4.1.2 Red wing absorption ([30,110] km s^{-1})

The right-hand panel of Fig. 5 shows the absorption in the red wing. All of our models present a more symmetric light curve with a maximum absorption around 10 per cent occurring in most of the cases half-hour after mid-transit. Only model H1, which is the one where planetary material falls towards the star, shows a deeper absorption that start about 4 h before than the optical transit. Contrary to the observations, none of our models reproduce the absorption detected between 2 and 4 h after mid-transit, implying that the neutral material moving towards the star remains up to a few planetary radii around the planet.

The absorption produced by our models can, in some cases, reproduce the absorption observed in the different wings of the Ly α line. But, individual models by themselves cannot fit all the observational data in both wings simultaneously. Given that the late absorption found in the red wing is from a different epoch than the early ingress found in the blue wing, we speculate that some of these features, specially the early absorption in the blue wing and the late absorption in the red wing, could be due to time-dependent events in the system that influences the interaction with the planetary wind.

4.1.3 Synthetic STIS line observation

The strongest (and most robust) feature of the Ly α observations happen in the blue wing and, with this in mind, models L1 and M3 are the ones that better reproduce the observations. To simulate an observation made with the STIS instrument, we convolved our Ly α profile (already attenuated by the ISM and absorbed by the neutrals) with the line spread function of the G140M grating. We show in Fig. 6 the Ly α line profile produced by model L1 at four different times: out of transit (black), 2 h before mid-transit (blue), at mid-transit (green), and 2 h after mid-transit (red) as shown in Ehrenreich et al. (2015). We also show in Fig. 6 what the in- and out-of-transit spectra would look like at high spectra resolution without any ISM attenuation or geocoronal contamination.

4.2 H α calculation

We obtained the H α synthetic transit profile using the same approach than for the Ly α calculations. The optical depth computation is as explained in Section 4.1, except that now we use the H α line parameters shown in Table 5. To estimate the population of neutral H atoms with electrons on the first excited level or $l = 2$ (with l denoting the energy level of the atom), we follow a similar approach to Christie, Arras & Li (2013) and we refer the reader to this paper for a more in-depth discussion. In summary, the physical mechanisms that are included in the calculations of the number density of atoms at $l = 2$, $\mathrm{n}_{l=2}$, are: the electron and proton collisional excitation and de-excitation, spontaneous radiative decay, photoexcitation and stimulated emission. We do not include recombination or photoionization from the second level, and as calculated for HD189733b by Christie et al. (2013) and Huang et al. (2017) they become negligible compared to other dominant processes such as radiative decay and photoexcitation.

Solving for the level 2 population is done at post-processing employing the *populate()* method within the subroutine *ch.ion()* in the CHIANTIPY package[2] (Dere et al. 2019). The *populate()* method computes the population of the different levels within an atom as a function of the temperature and the electron density including an external radiation flux. For the H α calculation we take the

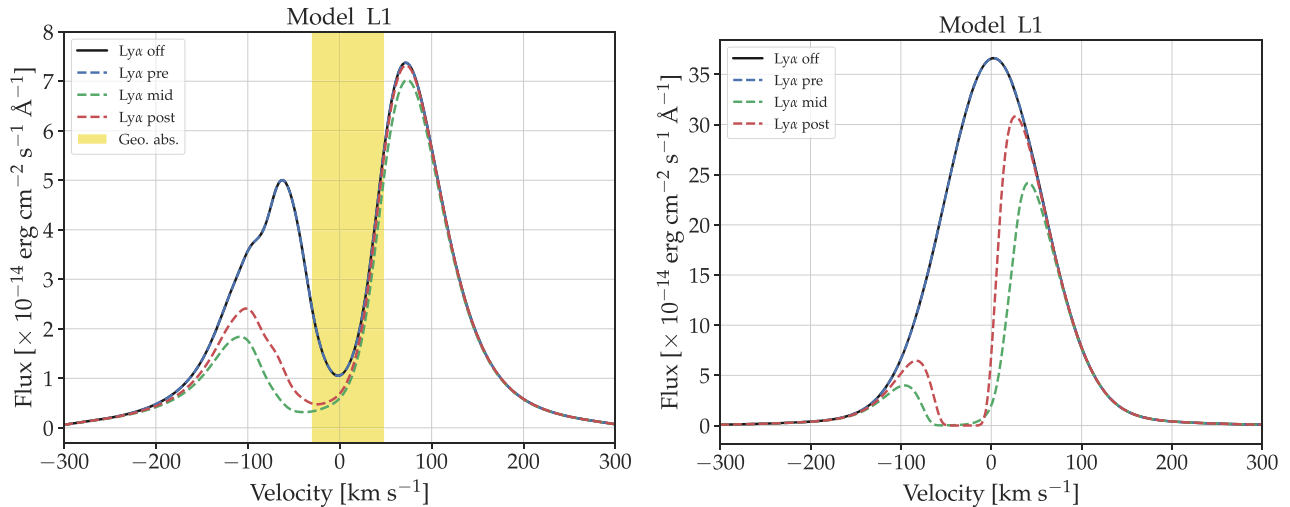[2]https://chianti-atomic.github.io/index.html

Figure 6. Ly α flux as a function of the velocity measured from the centre of the line in the stellar reference frame. The different lines represent the flux out of transit (filled black), 2 h before mid-transit (blue dashed), at mid-transit (green dashed), and 2 h after mid-transit (red dashed). The yellow stripe represents the part of the line contaminated with the geocoronal emission and interstellar absorption. The right-hand panel includes the effect of ISM attenuation along GJ 436's sight line and is convolved to match the STIS G140M resolution, and in the left-hand panel no ISM attenuation and high spectral resolution is assumed.

total number density of level 2 which is the sum of the levels 2s ($^2S_{1/2}$) and 2p ($^2P_{1/2}$ and $^2P_{3/2}$). We take the stellar Ly α flux as the external radiation field, by approximating it by a Planck function with temperature $T_{Ly\alpha,\star}$. We use $T_{Ly\alpha,\star} = 8150$ K, which gives almost the same value on average than the observed Ly α flux. This temperature resembles the chromospheric temperature found in the model of Peacock et al. (2019) for GJ 436 and is a larger than the 7000 K assumed for the solar-like star HD189733 in Christie et al. (2013) and more similar to the 8000 K adopted in Huang et al. (2017). As in Christie et al. (2013) we are also neglecting the attenuation, diffusion, and re-emission of the photons as they travel through the planetary material, otherwise, a full radiative transfer computation as the one done by Huang et al. (2017) should be included, and this is outside the scope of this work. The dilution factor for the external radiation field is $W = 0.5[1 - (1 - R_\star^2/a_p^2)^{1/2}]$, with $a_p/R_\star = 12.5$.

To compare with the observational results from Cauley et al. (2017), we compute the equivalent width of the H α line using

$$W_{H\alpha} = \sum_{v=-200}^{200} (1 - I_v/I_\star)\Delta\lambda_v,$$

where $\Delta\lambda_v$ is the wavelength difference at velocity v. We note that the integration is done in the velocity range ± 200 km s^{-1} as in Cauley et al. (2017).

The equivalent widths we compute for each of our simulations are shown in Fig. 7 as a function of time from mid-transit, with the grey band marking the duration of the optical transit. The observations from Cauley et al. (2017) are the pink data points, revealing no H α absorption. Fig. 7 shows that the absorption produced by our models is, in all cases, within the error and the dispersion found in the observation. Hence, we conclude that all of our models agree with the non-detection of H α absorption for this system.

Cauley et al. (2017) estimated that the ratio $N_{l=2}/N_{l=1}$, where $N_{l=2}$ is the column density of hydrogen atoms in the first excited level and $N_{l=1}$ the column density of H atoms in the ground state, should yield a value $< 10^{-3}$ in order for the absorption to be detected by the observations. Our computed values for the exited-to-ground-
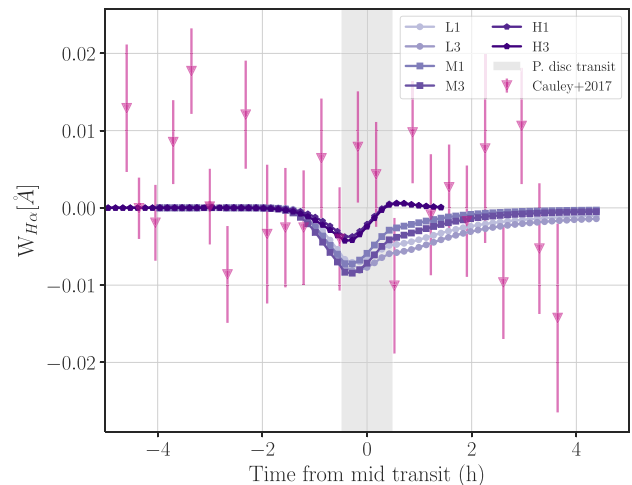

Figure 7. Equivalent width of H α as a function of time from mid-transit for all our models. The pink triangles show the observations from Cauley et al. (2017). The grey band represents the duration of the optical transit.

state ratios are around 4×10^{-7}, well below the upper limit estimation from Cauley et al. (2017).

5 DISCUSSION

In this work, we simulated the 3D interaction between the escaping atmosphere of GJ 436b and the wind of its host star. We explored different values of stellar wind strengths (given by base temperatures of 1 and 3 MK) and EUV luminosities ([0.8, 1.6, 4] $\times 10^{27}$ erg s^{-1}). From our set of 3D simulations, we constructed synthetic observations of the transit of GJ 436b in two hydrogen lines: H α and Ly α. In general, the interaction between the stellar and planetary winds resulted in a comet-like tail behind the planet and a shock ahead of the planet. The neutral material that leaves the planet's atmosphere is then distributed within this region and is responsible for the absorption seen in the Ly α line. Because this material is

asymmetrically distributed around the planet, the Ly α transit light curve is asymmetric, with different shapes depending on the EUV luminosity and stellar wind strength.

Overall, the Ly α absorption correlates more strongly with the stellar EUV flux in the blue wing – we found a larger absorption depth for lower EUV luminosities. In the red wing of the Ly α line, the stellar EUV flux does not have a great impact as most of the models give the same absorption depth. The absorption depth in the blue wing of the Ly α line is also dependent on the stellar wind strength. The stellar wind shapes the distribution of the material that leaves the planet and so, the absorption depth is larger for a stronger wind (considering the same L_{EUV}). The same behaviour can be seen in the red wing.

The maximum depth and the duration of the absorption light curve in the blue wing of the line (Lavie et al. 2017) is well reproduced by models L1 and M3. Model L1 has a low EUV luminosity and a stellar wind velocity of 254 km s^{-1} at the planet position, while model M3 represents a more moderate L_{EUV} value and a stronger stellar wind with a velocity of 465 km s^{-1} at the orbital distance.

The red wing absorption found after mid-transit is not properly reproduced by any of our models, as most of them produce rather symmetric light curves around mid-transit. The impossibility of fitting both red and blue absorption is also presented in Khodachenko et al. (2019).

The set of models with the larger L_{EUV} showed a different light curve in the blue wing. For these models a stream of material moving towards the star develops. Model H3 shows an early absorption in the blue wing of the line with a shallower depth and model H1 shows an early absorption in the red wing. In both cases, it is the material ahead of the planet the one producing the early ingress (also seen in Bourrier, Ehrenreich & Lecavelier des Etangs 2015).

However, these models cannot simultaneously reproduce the long-lived absorption seen after mid-transit in the blue wing. One possibility is that the early absorption might have been produced in a time variable event such as accretion of material towards the star occurring sporadically.

Contrary to the huge absorption observed in Ly α, GJ 436b does not show any significant absorption in the H α line. To compare with the observations, we computed the synthetic H α absorption from our models. We found that all our models give a non-detection of absorption during transit in agreement with the observations presented in Cauley et al. (2017).

5.1 Effects of charge exchange and radiation pressure in our simulations

The high-velocity component the Ly α line profile at high velocities (Fig. 6) are due to radiation pressure accelerating neutral hydrogen atoms and the stellar wind ram pressure that drags and accelerates planetary particles. One additional process that can contribute to this high-velocity component is charge exchange process, which we neglected in our models. We discuss some of these process below.

By running an extra set of simulations we investigated the role of radiation pressure in the models with the largest neutral density fraction at the planetary wind boundary (L1 and L3). A detailed analysis of these additional test simulations are seen in Appendix A1. By neglecting the radiation pressure, the effective gravity of the star is larger, which makes the planetary wind expand towards the star. The stellar wind provides the ram pressure necessary to stop this expansion. Thus, in the case of a weaker stellar wind (L1), this expansion (and consequent bow-shock formation) is stopped further away from the planet than in the case of stronger wind (L3). For case

L3, actually, radiation pressure affects very little the dynamics of the interaction, and thus the Ly α transit line profile is barely affected (see Fig. A3). For case L1, on the other hand, radiation pressure plays a larger role. This occurs because in this simulation the planetary wind neutral density is large and the stellar wind is not too strong.

Several authors have shown that radiation pressure does not play an important role in the case of HD 209458b and GJ 436b (among others Cherenkov, Bisikalo & Kosovichev 2018; Esquivel et al. 2019; Khodachenko et al. 2019; Debrecht et al. 2020). However, we have found here that this might not be always the case as it depends on the stellar wind and planetary wind parameters together with the flux in Ly α.

One limitation of our treatment is that our models do not include self-shielding of neutrals from the Ly α photons. With self-shielding, the stellar Ly α photon that is absorbed in a region of the planetary atmosphere can no longer contribute and thus radiation pressure weakens as one goes deeper into the planetary atmosphere. As a result, neglecting self-shielding leads to an overestimation of the radiation pressure in regions with a large amount of neutrals. In Appendix A2, we estimate the effect of neglecting self-shielding would have in our results. We found that this affects mostly the regions near the planet, where the planetary wind has smaller radial velocities. These regions only contribute to the Ly α transit near line center (± 30 km s^{-1}), which are excluded from the Ly α analysis due to geocoronal emission. Although they could be important for the H α analysis, the lack of absorption in this line also makes self-shielding not important. This is similar to what was concluded in the work of Esquivel et al. (2019) for HD 209458 and by Khodachenko et al. (2019) in the case of GJ 436.

Our models do not consider the processes of charge exchange. Inclusion of this phenomenon is well addressed by Khodachenko et al. (2019) in a multifluid simulation for GJ 436b. In their work, the authors attributed the blueshifted absorption in synthetic Ly α transits mainly due to charge exchange. Even though the effect of charge exchange has been modelled (approximately) in the past with single fluid simulations (Tremblin & Chiang 2013; Esquivel et al. 2019), we have chosen not to follow this path, because in order to have a realistic effect a multifluid treatment is necessary.

However, since charge exchange is produced near the shock between the stellar and planetary winds, adding this phenomenon to our models would have shifted the maximum absorption in the blue wing towards a time after mid-transit (as seen in fig. 10 of Khodachenko et al. 2019). The total amount of neutral material would remain the same, but the newly created neutral atoms would have the velocity of the stellar wind.

6 CONCLUSIONS

We have created a set of 3D models for the wind interaction in the exoplanetary system GJ436 varying the strength of the stellar wind and the stellar L_{EUV}. Based on spectroscopic transit observations, we explored different scenarios for the winds in the GJ 436 system. If we constrain our models based only on the Ly α observations of GJ 436b, we found that there is an ambiguity in the number of models that can reproduce these observations. In this case, models M3 and L1 can fit most of the observational points specially in the blue wing. However, we cannot disentangle which model is the best one. This degeneracy could be broken by using information from the synthetic H α transits. But, in the case of GJ 436b, all our models agree with the non-detection of H α absorption during the planetary transit.

Simultaneously fitting multiple observational diagnostics can help us constrain models to better derive physical parameters of planetary

systems. In this work, we aimed to fit two spectral lines (Hα and Lyα) observations with a unique model but, more than one model was able to reproduce the Hα observation making it hard to select our 'best' model. Based on the Lyα results, we conclude that the conditions of the stellar wind at the planet position are those determined by the values found in models L1 and M3: velocity $\sim[250 - 460]$ km s^{-1}, temperature of $\sim[4 - 3] \times 10^5$ K and a stellar mass-loss rate of 2×10^{-15} M$_\odot$ yr^{-1}. The stellar EUV luminosity for this model is set at $[0.8 - 1.6] \times 10^{27}$ erg s^{-1}, which produces a planetary mass-loss rate of $\sim[6 - 10] \times 10^9$ g s^{-1}.

DATA AVAILABILITY

The data underlying this article will be shared on reasonable request to the corresponding author.

REFERENCES

Allan A., Vidotto A. A., 2019, MNRAS, 490, 3760
Biro S., Raga A. C., Canto J., 1995, MNRAS, 275, 557
Bourrier V., Ehrenreich D., Lecavelier des Etangs A., 2015, A&A, 582, A65
Bourrier V., Lecavelier des Etangs A., Ehrenreich D., Tanaka Y. A., Vidotto A. A., 2016, A&A, 591, A121
Carroll-Nellenback J., Frank A., Liu B., Quillen A. C., Blackman E. G., Dobbs-Dixon I., 2017, MNRAS, 466, 2458
Cauley P. W., Redfield S., Jensen A. G., 2017, AJ, 153, 81
Cherenkov A. A., Bisikalo D. V., Kosovichev A. G., 2018, MNRAS, 475, 605
Christie D., Arras P., Li Z.-Y., 2013, ApJ, 772, 144
Debrecht A., Carroll-Nellenback J., Frank A., McCann J., Murray-Clay R., Blackman E. G., 2019, MNRAS, 483, 1481
Debrecht A., Carroll-Nellenback J., Frank A., Blackman E. G., Fossati L., McCann J., Murray-Clay R., 2020, MNRAS, 493, 1292
Dere K. P., Del Zanna G., Young P. R., Landi E., Sutherland R. S., 2019, ApJS, 241, 22
Ehrenreich D. et al., 2015, Nature, 522, 459
Ehrenreich D., Lecavelier Des Etangs A., Delfosse X., 2011, A&A, 529, A80
Esquivel A., Raga A. C., 2013, ApJ, 779, 111
Esquivel A., Schneiter M., Villarreal D'Angelo C., Sgró M. A., Krapp L., 2019, MNRAS, 487, 5788
France K. et al., 2013, ApJ, 763, 149
France K. et al., 2016, ApJ, 820, 89
Hazra G., Vidotto A. A., D'Angelo C. V., 2020, MNRAS, 496, 4017
Huang C., Arras P., Christie D., Li Z.-Y., 2017, ApJ, 851, 150
Khodachenko M. L., Shaikhislamov I. F., Lammer H., Berezutsky A. G., Miroshnichenko I. B., Rumenskikh M. S., Kislyakova K. G., Dwivedi N. K., 2019, ApJ, 885, 67
Kislyakova K. G. et al., 2019, A&A, 623, A131
Koskinen T. T., Harris M. J., Yelle R. V., Lavvas P., 2013, Icarus, 226, 1678
Kulow J. R., France K., Linsky J., Loyd R. O. P., 2014, ApJ, 786, 132
Lagrange A. M. et al., 1998, A&A, 330, 1091
Lammer H., Selsis F., Ribas I., Guinan E. F., Bauer S. J., Weiss W. W., 2003, ApJ, 598, L121
Lavie B. et al., 2017, A&A, 605, L7
Linsky J. L., Fontenla J., France K., 2014, ApJ, 780, 61
Loyd R. O. P. et al., 2016, ApJ, 824, 102
Loyd R. O. P., Koskinen T. T., France K., Schneider C., Redfield S., 2017, ApJ, 834, L17
Matsakos T., Uribe A., Königl A., 2015, A&A, 578, A6
McCann J., Murray-Clay R. A., Kratter K., Krumholz M. R., 2019, ApJ, 873, 89
Mesquita A. L., Vidotto A. A., 2020, MNRAS , 494, 1297
Murray-Clay R. A., Chiang E. I., Murray N., 2009, ApJ, 693, 23
Osterbrock D. E., 1989, Astrophysics of Gaseous Nebulae and Active Galactic Nuclei. University Science Books, Sausalito, CA
Peacock S., Barman T., Shkolnik E. L., Hauschildt P. H., Baron E., Fuhrmeister B., 2019, ApJ, 886, 77
Raga A. C., Cantó J., 1989, ApJ, 344, 404
Salz M., Schneider P. C., Czesla S., Schmitt J. H. M. M., 2015, A&A, 576, A42
Salz M., Czesla S., Schneider P. C., Schmitt J. H. M. M., 2016, A&A, 586, A75
Schneiter E. M., Esquivel A., Villarreal D'Angelo C., Velázquez P. F., Raga A. C., Costa A., 2016, MNRAS, 457, 1666
Shaikhislamov I. F., Khodachenko M. L., Lammer H., Berezutsky A. G., Miroshnichenko I. B., Rumenskikh M. S., 2018, MNRAS, 481, 5315
Shematovich V. I., Ionov D. E., Lammer H., 2014, A&A, 571, A94
Toro E. F., 1999, Riemann Solvers and Numerical Methods for Fluid Dynamics. Springer, Berlin
Torres G., 2007, ApJ, 671, L65
Trammell G. B., Arras P., Li Z.-Y., 2011, ApJ, 728, 152
Tremblin P., Chiang E., 2013, MNRAS, 428, 2565
Vidotto A. A., Bourrier V., 2017, MNRAS, 470, 4026
Villarreal D'Angelo C., Schneiter M., Costa A., Velázquez P., Raga A., Esquivel A., 2014, MNRAS, 438, 1654
Villarreal D'Angelo C., Esquivel A., Schneiter M., Sgró M. A., 2018, MNRAS, 479, 3115
von Braun K. et al., 2012, ApJ, 753, 171
Wood B. E., Linsky J. L., Hébrard G., Williger G. M., Moos H. W., Blair W. P., 2004, ApJ, 609, 838
Yelle R. V., 2004, Icarus, 170, 167
Youngblood A. et al., 2016, ApJ, 824, 101

APPENDIX A: THE EFFECT OF RADIATION PRESSURE IN OUR MODELS

A1 Comparison between models with and without radiation pressure

Here we investigate the effects that our implementation of the radiation pressure force has on our models. For this purpose we run a new set of simulation for models L1 and L3 without radiation pressure. In our setup this means we set $\beta = 0$ in equation (4). We choose these models as they are the ones with the highest neutral planetary density at the planet boundary condition, where we expect the effects of radiation pressure to be more noticeable.

Fig. A1 shows the radial velocity distribution in the orbital plane for model L1 with (left-hand panels) and without (right-hand panels) radiation pressure. Negative velocities, i.e. towards the star, cover a larger area for model without radiation pressure. This is a direct consequence of the larger effective stellar gravity now felt by the neutrals. Material being accelerated towards the star now shows a shock further from the planet in comparison with the model that includes radiation pressure. The lack of radiation pressure in model L3 (bottom panels of Fig. A1) has a less dramatic effect, with the
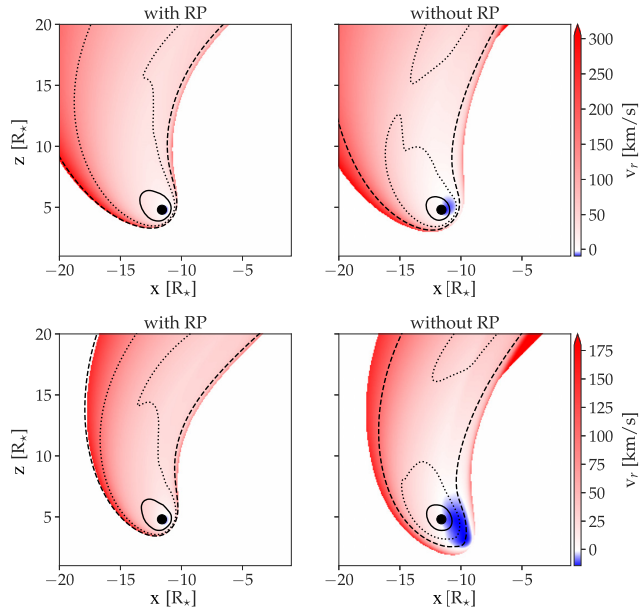
Figure A1. Radial velocity distribution in the orbital plane for model L1 (top) and model L3 (bottom) with (left-hand panel) and without (right-hand panel) radiation pressure. Velocities are measured from the stellar reference frame. Contours of ionization fraction are show in black: solid contour for 0.6, dashed for 0.8, and dotted for 0.9. The black filled circle shows the position of our boundary for the planetary wind ($5\,R_p$).

amount of material with negative velocities much closer and within a smaller region around the planet.

Because there is not much difference in the ram pressure of the planetary wind compared to the case with radiation pressure, the position of the shock does not change too much between these two models.

In the case where radiation pressure makes a more significant difference in the velocity distribution of neutrals (model L1), we also investigate the resulting Ly α profile during transit. Fig. A2 shows the absorption in both wings of the Ly α line as a function of time from mid-transit for the cases with (light blue lines) and without (orange lines) radiation pressure. Since part of the material that moves towards the star remains neutral (see the top right-hand panel of Fig. A1), the absorption in the red wing is larger compared to the case with radiation pressure. On the contrary, in the blue wing, the absorption has a smaller depth but starts a couple of hours earlier than in the case with radiation pressure. Also, when computing the line profile at mid-transit in Fig. A3, we can see that without radiation pressure, the profile is red shifted due to the neutral material moving towards the star, being more pronounce for model L1 (left-hand panel in Fig. A3) than in model L3 (right-hand panel Fig. A3).

From our test models, we have seen that radiation pressure acts on the densest regions of neutral material, and when it is not present, the planetary wind more easily expands towards the star. This behaviour is suppressed when the stellar wind ram pressure is strong enough to balance the planetary wind ram pressure at a closer distance to the planet, like in the case of model L3.

In model L1, the line profile at mid-transit shows a larger absorption at high negatives velocities when radiation pressure is included but there is not too much difference in model L3, when the stellar wind is stronger. This implies that in this last model, the stellar wind is mainly responsible for producing the blue-shifted high
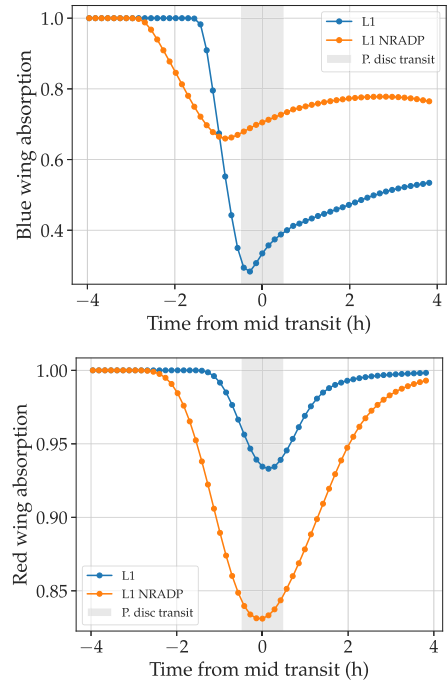

Figure A2. Blue ($[-120,\ -40]\,\mathrm{km\,s^{-1}}$) and red ($[30,\ 100]\,\mathrm{km\,s^{-1}}$) wing absorption in Ly α as a function of time from mid-transit for model L1 with (light blue lines) and without (orange lines) radiation pressure. The grey band represents the duration of the optical transit.
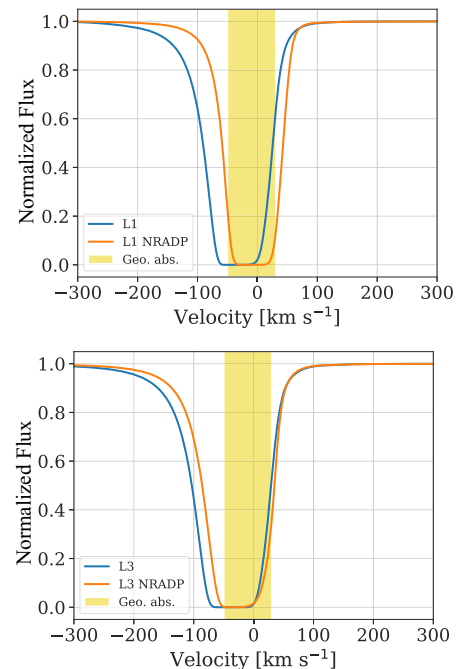

Figure A3. Normalized flux in the Ly α line as a function of velocity at mid-transit for model L1 (top panel) and L3 (bottom panel) with (light blue) and without (orange) radiation pressure. The signal is in the heliocentric reference frame. The yellow band shows the part of the line contaminated with the geocoronal emission.
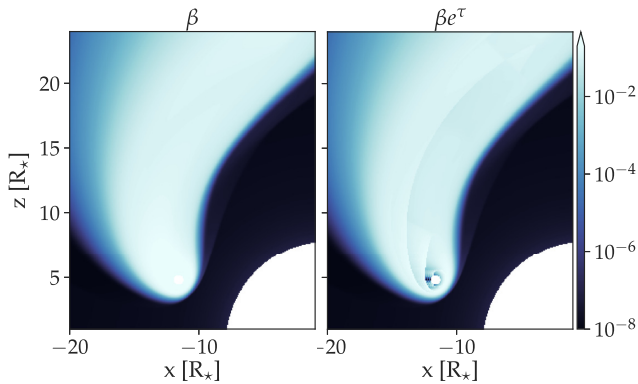
Figure A4. β value distribution in the orbital plane of model L1 without (left-hand panel) and with (right-hand panel) self-shielding. White circles are the boundary condition regions for the stellar wind and planetary wind.

velocity neutrals while in model L1 radiation pressure force is also responsible.

A2 Self-shielding

As we mentioned in Section 2.1, one caveat of our radiation pressure implementation is the lack of self-shielding. To study the influence of self-shielding in our models we have followed the same procedure as in Esquivel et al. (2019) and compute the attenuation of the Ly α flux due to the column density of neutral material in the path of the Ly α photon for different velocity bins. Even though this study is done as post-processing, since it will require a larger computational time to include self-shielding at real time, it gives us an idea of how much the radiation pressure within a cell changes if we allow the absorption (shielding) by neutrals.

The optical depth for this case is calculated by integrating the neutral column density from the star to the position of a given cell in velocity intervals, $\Delta v = 15 \, \mathrm{km \, s^{-1}}$:

$$\tau(v_{r,l}) = \frac{\sigma_0 \lambda_0}{\Delta v} \int_0^l n_\mathrm{H}(v_r, l') \mathrm{d}l', \qquad (A1)$$

where σ_0 is the absorption cross-section at the threshold wavelength and λ_0 is the Ly α central wavelength. Here, we are assuming that the line profile is a Delta function centred at the velocity $v_r \pm \Delta v/2$.

Fig. A4 shows the β value for model L1 as is used in our simulations (left-hand panel) and the resulting value when including self-shielding in post-processing (right-hand panel). We can see that β is reduced near the planet and in the inner regions of the cometary tail where the larger amount of neutrals are found. However, the largest attenuation is seen in a region very close to the planet where radial velocities are less than $30 \, \mathrm{km \, s^{-1}}$ (this conclusion was also found by Khodachenko et al. 2019). This velocity range is excluded from our Ly α transit calculations, as they belong to the Ly α region that is contaminated with the ISM absorption and the geocoronal emission. Thus, in our models, including self-shielding would only affect the regions of the Ly α line that is not observable. However, other systems might not behave as GJ 436 and thus to accurately see the effect of self-shielding, it is preferable to directly include it in the simulations.

Additionally, we can say that for model L1, the real distribution of the neutral material will be something between the cases with and without radiation pressure. Combined to the conclusions presented in Appendix A1, when the neutral density is small and/or the stellar wind is stronger, radiation pressure will be less important and neglecting self-shielding will have an even lesser effect in our results.

This paper has been typeset from a TEX/LATEX file prepared by the author.